Nuclear Inst. and Methods in Physics Research, A 943 (2019) 162436

Contents lists available at ScienceDirect

Nuclear Inst. and Methods in Physics Research, A

journal homepage: www.elsevier.com/locate/nima

Measurements of fast neutron scattering in plastic scintillator with energies from 20 to 200 MeV

W.F. Rogers [a,*], A.N. Kuchera [b,c], J. Boone [a], N. Frank [e], S. Mosby [d], M. Thoennessen [b,f], A. Wantz [a]

[a] Indiana Wesleyan University, Marion, IN 46953, United States of America
[b] National Superconducting Cyclotron Laboratory, East Lansing, MI 48824, United States of America
[c] Davidson College, Davidson, NC 28035, United States of America
[d] Los Alamos National Laboratory, Los Alamos, NM 87545, United States of America
[e] Augustana College, Rock Island, IL 61201, United States of America
[f] American Physical Society, Ridge, NY 11961, United States of America

ARTICLE INFO

Keywords:
Neutron detector
Plastic scintillator
Neutron scattering

ABSTRACT

Scattering of neutrons with energies ranging from 20 to 200 MeV was observed in an organic plastic scintillator array as a test for accuracy of simulation by two GEANT4-based models. The experiment was conducted at the LANSCE WNR facility at Los Alamos National Laboratory using a collimated neutron beam of well-defined energy and trajectory impinging on 16 BC-408 plastic scintillator detectors arranged in a horizontal array 2 detectors tall and 8 deep. Results from neutron scattering observations include hit-multiplicity distributions, beam attenuation depth, crosstalk events, scattering angle, attenuation depth between hits, and dark-scattering of neutrons from carbon nuclei, all as a function of the incident neutron energy. Measurement results are compared with predictions from two GEANT4-based Monte Carlo simulations, and agreement varies considerably over neutron energy, becoming poor at higher energies, pointing to needed improvement in simulation of neutrons in plastic scintillator.

1. Introduction

Fast neutron detection using organic plastic scintillator has proven to be an indispensable tool in the study of nuclei near the neutron dripline at laboratory facilities around the world, including NSCL/MSU (MoNA-LISA array) [1], GSI (NeuLAND array) [2], and RIKEN (NEBULA array) [3]. In these plastic scintillator arrays, neutrons are detected from light produced by recoil ionization as they scatter from H and C nuclei in the plastic. Light is typically collected using photomultiplier tubes. These detectors do not measure a neutron's energy directly, since only a portion of its energy is deposited at the scattering site. The neutron energy and momentum are obtained from time-of-flight between the point of production and the first scatter site, and the ray connecting the two. Neutrons often scatter multiple times in the detector volume, some scatters producing light above detector threshold and others below, making tracking of neutrons difficult.

The use of Monte Carlo simulation has been critical to the interpretation of data collected using scintillator arrays, enabling the detector response function to be adequately accounted for in the extraction of meaningful physics results. As experimental studies of exotic nuclei continue to advance in sensitivity and sophistication, they will increasingly rely on simulation for the extraction of weak signals, such as in systems involving multiple neutron decays [4–7], where the background from single neutron scattering can mask the weaker multiple neutron signal.

Experiments using MoNA-LISA at NSCL have typically measured neutrons in the 40–100 MeV range, while the next generation accelerator at the Facility for Rare Isotope Beams (FRIB) [8] will soon come online with higher beam energies, producing neutrons with energies up to 200 MeV. Motivation for the work reported here is to assess the accuracy of Monte Carlo simulation for several key neutron scattering signatures, not only to improve the analysis of current experiments, but more importantly to prepare for the next generation of experiments at FRIB.

2. Neutron detection with the MoNA-LISA arrays at NSCL

The Modular Neutron Array (MoNA) [1] and the Large multi-Institutional Scintillator Array (LISA) are located at the National Superconducting Cyclotron Laboratory (NSCL) at Michigan State University, each consisting of 144 (10 cm) × (10 cm) × (200 cm) BC-408 (MoNA) or Eljen EJ-200 (LISA) plastic scintillator detectors, stacked in either compact or open arrays (see Fig. 1). Photonis XP2262B photomultiplier tubes (PMTs) coupled to opposite ends of the detector measure the

* Corresponding author.
E-mail address: warren.rogers@indwes.edu (W.F. Rogers).

https://doi.org/10.1016/j.nima.2019.162436
Received 29 April 2019; Received in revised form 15 July 2019; Accepted 22 July 2019
Available online 30 July 2019
0168-9002/

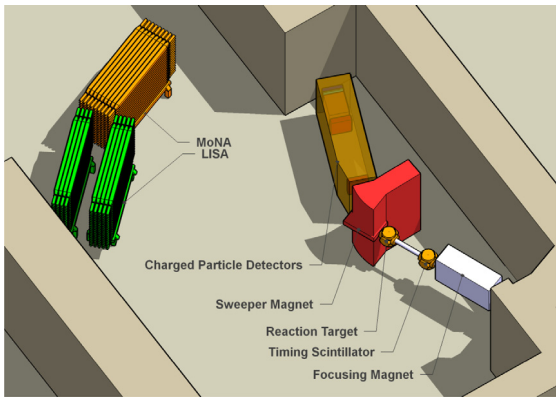

Fig. 1. Recent layout of the MoNA and LISA arrays in the N2 vault at NSCL, including the reaction target, Sweeper Magnet, and charged-particle detector chamber.

Table 1
Cross sections and Q-values for the most common neutron scattering interactions with H and C nuclei in plastic scintillators. Data are for 90 MeV neutrons [12,13]. The last column lists those scattering channels for which cross sections (approximate in some cases) are used in MENATE_R [14].

Reaction	σ (mb)	Q Value (MeV)	Product	Menate_R
^{1}H(n,n′)p	80	0	n	yes
^{12}C(n,n′)^{12}C	250	0	n	yes
^{12}C(n,2n′)^{11}C	22	18.72	2n	yes
^{12}C(n,n′)^{12}C + γ	14	4.43	n, γ	yes
^{12}C(n,p)B + Xn	95	12.59	Xn	yes
^{12}C(n,d)B + Xn	24	15.96	Xn	yes
^{12}C(n,n′)3α	39	7.28	n	yes
^{12}C(n,α)^{9}Be	4	5.71	0n	yes
^{12}C(n,X)2α	28	n/a	3n	
^{12}C(n,X)Li	40	n/a	Xn	

arrival time difference for scintillation light, enabling position sensitivity along the 200 cm length. Position resolution (FWHM) for the detectors ranges from 10 cm (for 20 MeV neutrons) to 6 cm (for 200 MeV neutrons), and these values were incorporated into simulation calculations (see Section 4.1).

The arrays have typically been used to measure the trajectory and time-of-flight for neutrons resulting from decay of unbound nuclei at the neutron dripline, produced by nuclear reactions in inverse kinematics. These in turn allow determination of their energies and momenta. Charged fragments from the decay are bent away from the beam direction by a 4-T Sweeper Magnet [9]. The fragments then enter a suite of charged particle detectors which determine their mass, charge, trajectory, and time-of-flight, which then determine their energies and momenta. The full neutron-fragment system 4-momentum is determined on an event-by-event basis, allowing reconstruction of the decay dynamics using invariant mass spectroscopy to determine masses and energy level structure for these unbound nuclei.

For experiments involving single-neutron decays, the first hit in the array is sufficient to determine the energy and momentum of the neutron. For experiments involving multiple-neutron decays, the challenge is to discriminate between signals arising from a multi-neutron event and from a single neutron scattering multiple times. Various "causal" filters have been employed [4–7,10,11] in an attempt to increase the multi-neutron event signal-to-noise ratio. These filters typically use the measured distance and velocity between the first two hits, which for single neutron scattering are causally related via energy and momentum conservation. We will return to this topic in Section 5 with discussion of potential improvements for single neutron causal filters.

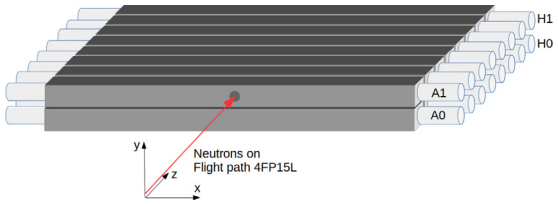

Fig. 2. The detector array geometry used in this experiment. The lower layer detectors are labeled A0 to H0 and the upper layer A1 to H1. The coordinate system used for our analysis is also shown. The neutron beam strikes the array along the center normal of detector A1.

2.1. Neutron scattering in BC-408

The H to C ratio in BC-408 scintillator (Polyvinyl toluene) is 1.104:1 and its density is 1.023 g/cm^3 [15]. Table 1 lists the most common neutron interactions in MoNA-LISA and their cross sections [12,13] for 90 MeV neutrons. Only data for neutrons scattering from ^{1}H and ^{12}C are included in the table and in simulation owing to the very low abundance of other H and C isotopes in the plastic. Over the range of neutron energies presented here (20 MeV to 200 MeV) elastic scattering from C nuclei (and some inelastic scattering channels as well) produce light below typical scintillator detector thresholds, thus constituting "dark-scattering", which alters neutron trajectories without detection. The variety of possible neutron interactions with C nuclei, and the different resulting scattering dynamics, light production, and extra particle production (neutrons, alphas, gammas) makes tracking of individual neutrons difficult. Elastic scattering of neutrons from H nuclei is comparatively simple, resulting in light produced by direct as well as by charge-exchange scattering. A 90 MeV neutron in the detector volume is three times more likely to elastically scatter from C (dark) compared with scattering from H (light).

3. Experimental details

The experiment was conducted at the Weapons Neutron Research (WNR) facility [16] at Los Alamos Neutron Science Center (LANSCE) [17] at Los Alamos National Laboratory. A total of 16 detectors from the MoNA array were placed in the 90-m station on the 4FP15L flight path, and arranged in an array 2 detector bars tall and 8 bars deep, as shown in Fig. 2. The lower layer detectors (starting from the front) are labeled A0 to H0, and the upper are labeled A1 to H1. The neutron beam entered the upper layer along the surface normal, 1.3 cm above the center point of bar A1.

3.1. Data acquisition

Data were collected with three CAEN VX1730B 500 MS/s digitizers (using PHA firmware) mounted in a VME64X crate, one dedicated to the 16 left PMTs, one dedicated to the 16 right PMTs, and one for the T_0 signal corresponding to the timing of proton beam pulses on the spallation target for neutron time-of-flight calibration. All digitizer channels triggered independently using channel specific digital constant fraction discrimination (CFD) settings. Neutron detectors were set to a common trigger threshold after the hardware-level gain matching was complete. Each channel therefore generated independent firmware events when their individual trigger thresholds were satisfied. Each firmware event consisted of a 47-bit trigger timestamp which was discrete at the 2 ns level, an interpolated time based on the digital CFDs to obtain sub-2 ns timing, and two charge integrals. Detector light thresholds were digitally set to 1 MeVee.

All channels within a single digitizer module track a common phase lock loop (PLL) clock and are therefore synchronized. For this measurement, board zero served as the master PLL clock. This clock was propagated via clock connections on the front face of the digitizer to

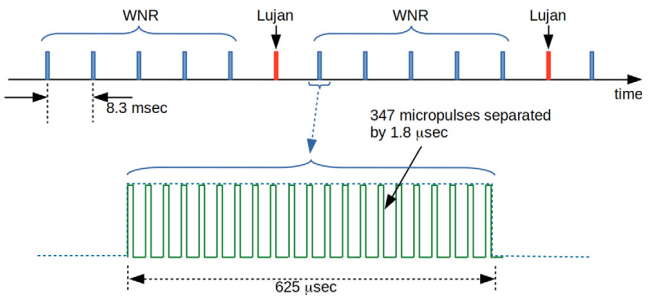

Fig. 3. Proton beam pulse structure used for the production of spallation neutrons at LANSCE. Every second 120 macropulses of 800 MeV protons, each lasting 625 μs and separated by 8.3 ms, are directed onto two separate spallation targets, 100 of them to the WNR target and 20 to the Lujan Center target. The Lujan pulses are evenly spaced, so the WNR pulses occur in groups of 5 macropulses separated by 1 missing pulse. Each macropulse contains 347 micropulses of duration 1.8 μs.

the next digitizer in line, which both locked on to the clock and passed it to the next board in a daisy chain, thus locking all channels to the master PLL clock. The firmware output had no inherent physics event structure, so time ordering and physics event building were therefore done in software.

3.2. Neutron beam rates and pulse structure

The neutron beam entered the 90-m station through a 3-mm collimator, produced upstream by spallation from 800 MeV protons directed onto a Tungsten target, located approximately 90 m away. The proton beam was produced by the LANSCE 800 MeV linear accelerator operating at 120 Hz. Each 8.33 ms beam cycle consisted of a 625 μs macropulse of modulated proton beam followed by beam silence for the remainder of the cycle. Five out of six proton beam macropulses were directed to the WNR facility target, while every sixth macropulse was directed to the neighboring Lujan Center, which provides neutron beams for low energy experiments [18]. Hence, neutrons entered the 90-m station in 100 macropulses per second, each macropulse consisting of 347 micropulses. Each micropulse consisted of approximately 200 ps of proton beam on the spallation target [19], followed by 1.8 μs of beam silence before the next pulse, during which spallation neutrons of all energies moved out from the target. This pulse and timing structure resulted in a neutron beam livetime of 62.5 ms/s. A brief schematic of this timing scheme is depicted in Fig. 3.

3.2.1. Wrap-around neutrons

Low energy neutrons too slow to reach the detectors within the 1.8 μs micropulse window in which they were produced enter the 90-m station in one of the following micropulse windows, alongside prompt neutrons of higher energy. These wrap-around neutrons constitute a low-energy source of background for prompt neutrons, and were filtered out by requiring that detector light produced by the first hit be above the wrap-around kinetic energy equivalent. Subsequent hit thresholds were digitally set to 1 MeVee. Fig. 4a shows the wrap-around neutron kinetic energies corresponding in time to prompt neutrons of higher energy.

3.2.2. Two-neutron event probability

The majority neutron scattering events in the array are single neutron (1n) events. Some fraction of the time we expect two prompt spallation neutrons (2n) to enter the room during the same micropulse, constituting background for 1n events. We used the observed beam rates within well-defined neutron energy windows $(E \pm (0.05)E)$ to estimate the 2n rate using Poisson statistics. The probability ratio $P(2n)/P(1n)$ is shown in Fig. 4b, which corresponds to the 2n event probability relative to 1n probability in the same time-of-flight window, for neutron energies ranging from 20 to 200 MeV. We judged the 2n event probability to be low enough not to constitute a background concern for all neutron energies considered.

3.3. Neutron beam characteristics

The distance from the spallation target to the front face center of detector A1 was 88.63 m. Neutron kinetic energy was determined using the time-of-flight from the spallation source to the point of first light detection in the array, using a T_0 timing signal produced by beam electronics synced to the proton beam pulses. The arrival time of prompt gamma rays produced at the spallation target were used to calibrate neutron time-of-flight, which allowed determination of the neutron kinetic energy. Fig. 5 shows the neutron time-of-flight and kinetic energy distributions for a typical run. The background level on the left side of the time-of-flight plot is from wrap-around neutrons.

Neutron beam countrates ranged from approximately 7/s for 20 MeV neutrons to approximately 80/s for 200 MeV neutrons. Both of these rate measurements are for events whose first-hit light is above the wrap-around energy threshold (Section 3.2.1).

3.4. Sources of background

The following constitute additional sources of background for our measurements, which include scattered beam, detector bar activation, and cosmic muons.

3.4.1. Scattered beam

A fraction of neutrons entering the 90-m station were scattered by the collimator into large angles, illuminating the array approximately uniformly, with a similar energy distribution to that of beam neutrons. We observed that a fraction of first hit events occurring in lower layer detectors (which were not in the path of the beam) produced a similar light output over their entire lengths, attenuation depth, and crosstalk behavior as observed for beam neutrons.

An estimate of rate for these scattered neutrons was obtained by comparing the countrate in the middle ±10 cm of the front upper and lower detector bars, filtered to reduce the contribution of crosstalk events (where a scattered proton produces light in each of two adjacent bars — see Section 4.4.2). The scattered beam flux over the middle ± 10 cm range in the lower detector was determined to be less than 1% of that for the same ± 10 cm in the upper detector which includes the beam, for neutrons from 20–200 MeV. An algorithm used to minimize the contribution of these scattered neutrons to dark-scattering observations will be described in Section 4.4.3.

3.4.2. Detector bar activation and epi-thermal room neutrons

Each macropulse was followed by a period of beam silence (see Section 3.2) during which detector counts persisted briefly, falling in intensity in an exponential-like fashion with a short lifetime component of around 1 ms and a longer lifetime component of 10's of ms. The short component was determined to arise mainly from wrap-around neutrons still entering the room after the macropulse end, and possibly the die-out of epi-thermal neutrons scattering in the room. The longer component was determined to arise from neutron activation in the bars, which includes contribution from the production of beta-unstable ^{12}B (lifetime ≈30 ms) via neutron charge-exchange from C. These events were most intense along the neutron beam path. Countrates for these two decay components were low compared to typical datarates, and the light produced for both was largely below the wrap-around energy threshold, leading us to conclude that they did not constitute a background concern for first hit events.

3.4.3. Cosmic muons

Cosmic muons enter the room with predominantly vertical trajectories and deposit approximately 2 MeV/cm for a total of 20 MeV or more depending on angle. The large majority of muon-induced events produce coincidences between the upper and lower layers.

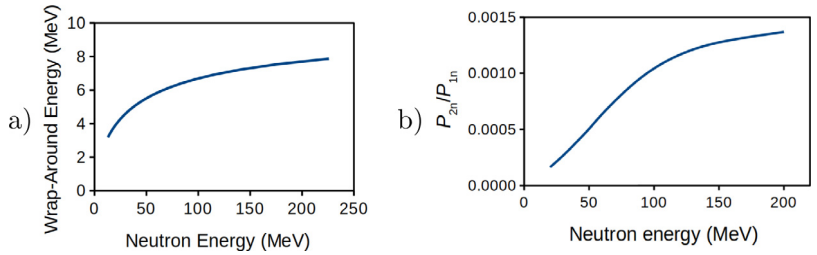

Fig. 4. (a) Computed wrap-around neutron energy as a function of prompt neutron energy for the 90-m station at the LANSCE WNR facility. (b) Computed 2n probability relative to that for 1n, plotted as P_{2n}/P_{1n} *vs*. neutron energy.

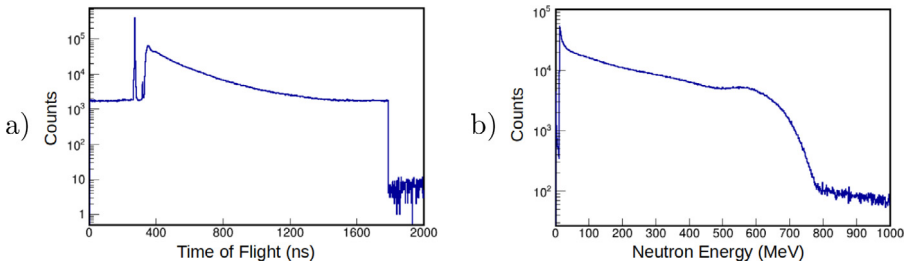

Fig. 5. (a) Time-of-flight spectrum for neutrons entering the 90-m station. The spike at 300 ns corresponds to prompt gamma-rays produced at the spallation target, and is used for time calibration of the neutrons. (b) Neutron energy spectrum, computed from time-of-flight. Note the cutoff at 800 MeV, corresponding to the highest energy protons on the spallation target.

4. Scattering observations

4.1. Test for two GEANT4-based simulation approaches

We compared experimental observations for several key scattering observables with two GEANT4-based [20] simulation model predictions. A dedicated physics list was implemented in our ST-MoNA code that uses GEANT4 version 4.9.3.p02 and combines the standard electromagnetic physics package (G4EMStandardPhysics_option_3 [21]) with two options to treat neutron physics: one based on the Japanese evaluated neutron data library (JENDL) [22] and one based on the MENATE_R [23] neutron scattering cross sections.

The first, which we refer to as G4-Physics, uses the stock GEANT4 physics classes to model neutron interactions in the detector volume. Neutrons below 20 MeV were modeled using high precision neutron transport models [20], derived from the Evaluated Nuclear Data Files (ENDF/B-VI) [24,25]. For neutrons above 20 MeV, cross sections for elastic scattering from H nuclei, and elastic and inelastic scattering from C nuclei were drawn from the JENDL library [22,26] for neutrons ranging in energy from 20 MeV to 3 GeV.

The second model, which we refer to here as MENATE_R, is used within the GEANT4 framework and based on MENATE [23], which was used to model neutrons in NE213 scintillator. Elastic neutron scattering cross sections from H and C nuclei above 20 MeV are drawn from references [13,27], while below 20 MeV they are drawn from the ENDF/B-VI database [24,25]. Inelastic neutron scattering cross sections from C nuclei are drawn from references [13,27]. Available cross section data for neutron inelastic scattering from C nuclei are sparse for energies ranging from 20 to 200 MeV [13], limiting the effectiveness of this cross section-based approach. Modeling for these inelastic channel contributions uses the best estimate for their total cross section as a function of energy, and scattering is modeled as isotropic in the center-of-mass frame. Improved data for these inelastic scattering channels would benefit simulation efforts and potentially improve their accuracy. Angular distributions for elastic scattering from H and C nuclei are included in both model calculations.

Both models incorporate details of the geometric and physical makeup of the detectors, including the BC-408 scintillator material, vinyl wrapping, and acrylic light guides. The neutron beam was modeled in GEANT4 to match the momentum and energy characteristics of the experimental beam emerging from the 3 mm collimator, with the same entry point near the middle of bar A1. Neutron interactions with H and C nuclei were translated into light production in the scintillator volume using the Birks formula [28] for each particle producing light in the detector. On the low energy side, the Birks formula was used to reproduce the Compton edge from a γ-ray source, and on the high energy side, light signal endpoints for data and simulation were matched for each neutron energy window considered. Light attenuation along the length of the scintillator bar was measured and parameterized, and incorporated into simulation. Similar detector thresholds were applied to data and to simulation, which for first hits in the array were set quite high in order to remove the contribution from wrap-around neutrons (see Section 3.2.1). Any additional analysis gates applied to experimental data were also applied to the two simulations.

4.2. Related work

Kohley et al. [29] analyzed data from a MoNA-LISA experiment on the single neutron decay $^{16}\mathrm{B} \rightarrow {}^{15}\mathrm{B} + \mathrm{n}$ produced by a proton knockout reaction from a 55 MeV/u ^{17}C beam, in order to test and compare the same two GEANT4-based [30,31] simulation packages relative to their experimental observations.

They concluded that the MENATE_R model was better able to replicate experimental observations for 55 MeV neutrons compared with the G4-Physics cascade model. Large discrepancies observed between the two models were believed to arise from the different ways in which each treat the inelastic C scattering channels. Their analysis was limited to 55 MeV neutrons arising from nuclear decay, whose trajectories were largely indeterminate as they interacted with the detector array. The current experiment benefits from a much broader neutron energy range with well-defined trajectory and entry point in the array. In Section 4 we will compare our experimental scattering observables with predictions from these same two GEANT4-based models.

While both models use neutron scattering cross section data, the main difference between them is in how they treat the inelastic scattering channels for C nuclei. MENATE_R uses the discrete inelastic scattering channels by drawing from experimentally determined cross section data. G4-Physics uses the total inelastic scattering cross section (derived from the JENDL database) and then computes the outgoing neutron kinematics using the cascade model within GEANT4.

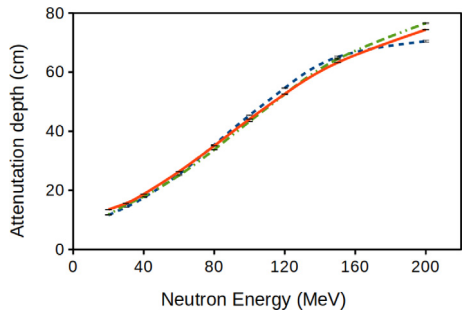

Fig. 6. Neutron beam attenuation depth in the detector array. The solid curve (red) corresponds to data, the dashed (blue) to MENATE_R model prediction, and dot–dash (green) to G4-Physics model prediction. All error bars are statistical.

4.3. Important analysis gates

Two sources of background requiring analysis gates include collimator-scattered neutrons (Section 3.4.1) and wrap-around neutrons (Section 3.2.1). In order to reduce the contribution of scattered-beam initiated events, we applied a "beam" gate, defined as the requirement that a first hit be within $x = \pm 5$ cm of any upper layer bar center. In order to filter signals produced by wrap-around neutrons, we applied a "wrap-around" gate, defined as the requirement that light produced by a first hit be above the threshold corresponding to the wrap-around neutron's kinetic energy. The value for this threshold is a function of neutron energy (see Fig. 4). Light thresholds applied to subsequent hits were set to 1 MeVee. Unless noted otherwise, the beam and wrap-around gates were applied to all analysis.

4.4. Events satisfied by a single scatter

Scattering observables satisfied by at least one detected neutron scatter in the array include attenuation depth for the neutron beam, proton crosstalk between adjacent detectors, neutron dark-scattering via elastic scattering from C nuclei, and event multiplicity distribution.

4.4.1. Neutron beam attenuation depth

The interaction rate for the neutron beam drops with depth as the beam attenuates in intensity. The attenuation depth is defined as the depth by which the initial beam intensity (as measured by the first hit rate) drops by the factor $1/e$. We measured the beam attenuation depth for neutron energies from 20 to 200 MeV. Fig. 6 shows the attenuation depth for neutrons over this energy range for both data and the two model predictions. Both simulations do a good job modeling attenuation of the neutron beam.

4.4.2. Proton crosstalk between adjacent detectors

Neutron charge-exchange scattering (n,p) from H and C nuclei produces high-energy protons moving predominantly in the forward direction. As incoming neutron energy increases, so does the energy of the scattered proton, and therefore the probability that the proton will produce additional light in the next detector downstream, illuminating both detectors nearly simultaneously. These proton crosstalk events appear as multiplicity 2 to the DAQ, though they originate from a single neutron scatter. A small fraction of the time these events are processed in reverse time order, owing to finite detector and electronics timing resolution.

We measured the rate for proton crosstalk events and compared it to the rate for all hit-multiplicity 1 events (which they are), and to the rate for all hit-multiplicity 2 events (which is how they appear to the DAQ). Fig. 7 shows the ratio of these rates for horizontal crosstalk between adjacent detector bars for neutrons with energies from 30–200 Mev. Analysis was limited to multiplicity 2 events, and scattering in the upper layer only.

As seen in Fig. 7, both models overpredict the rate of horizontal proton crosstalk events. MENATE_R does the better overall job predicting the trend. Data for neutrons above 150 MeV suggest that crosstalk events (appearing to the DAQ as hit-multiplicity 2) approach a rate of 1/3 that for hit-multiplicity 1 events. The curves begin to flatten out above 120 MeV because by this energy charge-exchange protons have sufficient energy to begin connecting three consecutive bars via crosstalk. Gates using crosstalk events can be used to filter 1n events from a 2n event dataset, to be discussed in Section 5.2.

4.4.3. Dark scattering — elastic scattering of neutrons from C nuclei

The elastic scattering cross section for neutrons from C nuclei, which for the energies considered here constitute dark-scattering, is the highest of those listed in Table 1. Detection of dark-scatter events is a challenge because by definition the first actual scatter remains unrecorded, so its location cannot be known in order to evaluate the neutron's scattering behavior. Dark-scattering redirects a neutron's trajectory without record, and in this way serves to decrease the array's position resolution. This in turn translates into a loss in kinetic energy and trajectory resolution for the neutrons.

When the neutron beam enters the upper layer of the array, some of the dark-scattered neutrons will illuminate the lower layer. We looked for multiplicity 1 events in the lower layer, above the wrap-around threshold. The multiplicity filter eliminates time-reversed proton crosstalk events coming from one of the bars above. To reduce background from the collimator-scattered beam neutrons, the light distribution along the length of the lower front detector A0 (filtered using the same analysis gates) was subtracted from the light distribution of all other lower detectors, appropriately scaled for depth attenuation.

Fig. 8 shows an overhead view of the intensity pattern in the lower layer bars resulting from 80 MeV neutrons dark-scattered from the

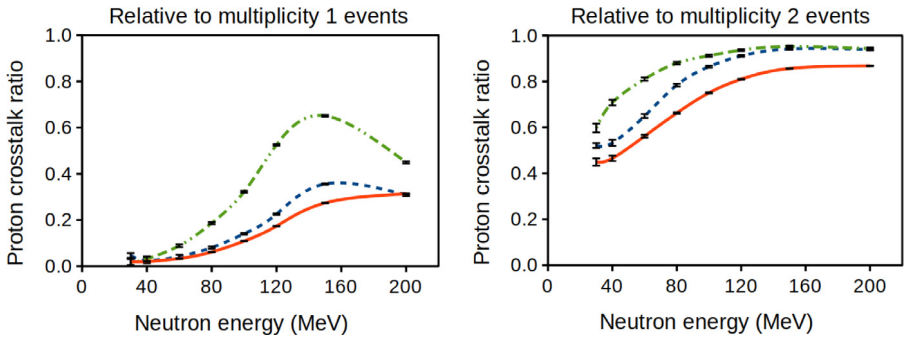

Fig. 7. Contribution of horizontal proton crosstalk events connecting adjacent bars in the upper layer of the array, expressed as a fraction of all hit-multiplicity 1 (left) and hit-multiplicity 2 (right) events. The solid curve (red) corresponds to data, the dashed (blue) to MENATE_R model prediction, and dot–dash (green) to G4-Physics model prediction. All error bars are statistical.

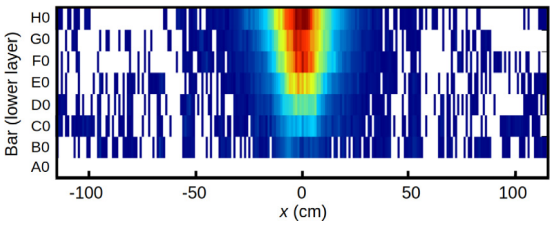

Fig. 8. Overhead view of interactions in the lower layer bars produced by 80 MeV neutrons dark-scattered from the upper to the lower layers. Along the vertical axis is depth in the array indicated by the bar labels, where A0 is at the front and H0 is at the back of the array. Along the horizontal axis is position along the bar's length. The neutron beam enters the array vertically from below at bar center.

upper layer. Position along the bar's length is plotted on the horizontal axis. The neutron beam enters from below at the array center point.

Dark scattering results for 20 to 80 MeV neutrons are shown in Fig. 9. A schematic for the measurement is shown in Fig. 9(a) for the array in profile, and results for neutrons dark-scattered from the upper to the lower layers are shown for four neutron energies in Fig. 9(b). Labels corresponding to lower layer detector bars appear on the x-axis (where A0 is the front and H0 is the rear detector), and the rate for neutron dark-scattering to the lower layer detectors appears on the y-axis, relative to the rate for all light producing events of all multiplicities. Bar A0 was not included in this measurement since its light pattern was used to filter collimator-scattered neutrons from the rest of the lower layer detector signals, and it receives very little dark-scattering from detector A1.

Data shown in Fig. 9 cover a scattering angle range from approximately 10° to 45°. A rough estimate for dark-scattering probability can be made assuming that the solid angle for the illumination pattern in the lower layer (see Fig. 8) represents 25% of the complete solid angle cone centered on the beam axis. Based on this rough assumption, integration of the experimental curves in Fig. 9 leads us to conclude that approximately 15% of 20 MeV neutrons dark-scatter between 10° and 45° (relative to all light-producing events of all multiplicities), down to 12% for 200 MeV neutrons. As the data also show, dark-scattered neutrons become increasingly forward-focused at higher energies, so that by 200 MeV most dark-scatters appear to be directed beyond the back end of the array, at angles less than 10°.

Both models generally overpredict the dark-scattering probabilities from 20 to 80 MeV. The MENATE_R model predictions more closely match our experimental observations, especially well at 40 MeV. A different detector array geometry optimized for dark-scatter observations would be better able to characterize the angular distribution as a function of neutron energy.

4.4.4. Multiplicity distributions

Multiplicity distributions for single neutron (1n) scattering in the detector array were measured as a function of incoming neutron energy and compared with both model predictions. Fig. 10 shows a plot of the ratio of simulation prediction to data for event multiplicity, normalized to multiplicity 1 values.

The MENATE_R model predictions reproduce multiplicities 2 to 4 well for neutrons with energy between 30 and 120 MeV, and poorly outside that range. G4-Physics model predictions are poor, especially for neutrons with energies above 80 MeV.

4.5. Events satisfied by two or more scatters

In order to model the propagation of neutrons between first and second light-producing interactions in the array, simulation must accurately model the first scattering event in terms of energy deposited and redirection of the neutron's trajectory (in addition to the possible production of extra particles), followed by propagation of the neutron in the scintillator medium to its next hit. Two experimental signatures

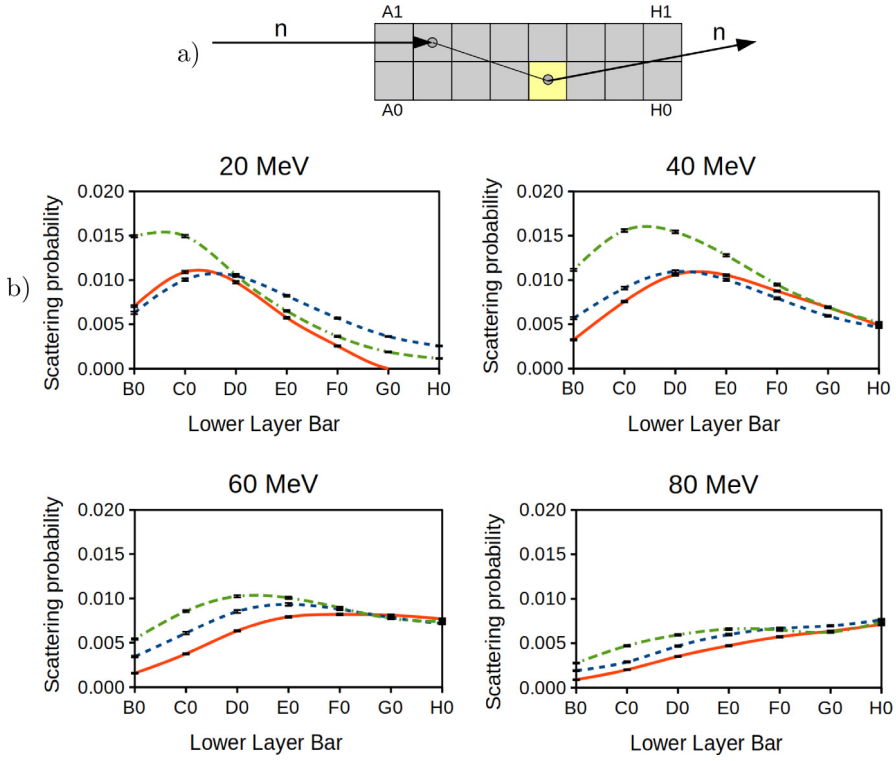

Fig. 9. (a) A side view of the detector array with an example of a neutron dark-scattering from the upper to the lower layer. Only the second interaction, occurring in the lower layer, is detected. (b) Dark-scatter pattern for neutrons scattered from upper bars to lower bars for 20, 40, 60, and 80 MeV incident neutrons, and simulation results for comparison. Solid curves (red) are data, dashed curves (blue) are MENATE_R simulation prediction, and dot-dashed curves (green) are G4-Physics simulation prediction. All error bars are statistical.

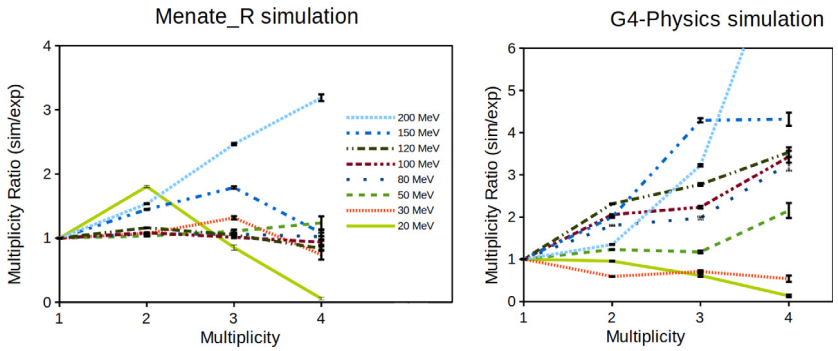

Fig. 10. The ratio of G4-Physics and MENATE_R model predictions relative to experimental observations for hit-multiplicity in the array, normalized to multiplicity 1 rates. Note that the plots have different y-axis scaling. All error bars are statistical.

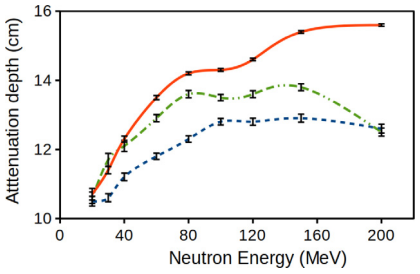

Fig. 11. Attenuation depth between hits 1 and 2 in the upper layer of the array. Scattering intensity for second hits drops by the factor $1/e$, or 37%, by this distance from the first hit. Solid curve (red) corresponds to data, the dashed curve (blue) to MENATE_R simulation, and dot-dashed curve (green) to G4-Physics simulation. All error bars are statistical.

used to test model predictions for neutron propagation in the medium include attenuation depth between first and second hits, and scattering angle defined by the incoming and outgoing neutron trajectories. For analysis of both observables we required that the first and second hits be constrained to the upper layer detectors, in part to filter out contribution from cosmic muons, and in part to observe smooth variation in the observables and avoiding abrupt angle changes from upper to lower layer scattering.

4.5.1. Attenuation depth between hits

Fig. 11 shows results for the attenuation depth between the first and second hits for experiment and for the two model predictions. We added the additional analysis requirement that separation between the first and second hit be 20 cm or greater, in order to reduce or remove the contribution from crosstalk events whose contribution (especially at higher neutron energies) biases the dataset toward distances near 10 cm. The G4-Physics model reproduces the attenuation depth well for energies below 100 MeV and poorly above it, while the MENATE_R model reproduces the data poorly over the entire energy range. Modeling the neutron propagation between hits is important to the development and use of causal filters designed to increase the signal-to-noise for multiple neutron events, to be discussed in Section 5.

4.5.2. Scattering angle

Fig. 12 shows the measured scattering angle probability from 0 to 90° for incoming neutrons with energy from 20 to 200 MeV (each with a ±5% window). Additional gates applied to this analysis include the requirement that hits 1 and 2 be separated in z by at least 1 bar between them, in order to eliminate crosstalk contributions. Plotted on the horizontal axis is θ_{12}, defined as the scattering angle in range $\theta_{12} \pm 5°$ at which a neutron scatters between hit 1 and hit 2 relative to the incoming neutron beam direction. Plotted on the vertical axis is the scattering probability relative to all detected events of at least multiplicity 1. For example, a value of 0.0075 on the 200 MeV data curve at 10° means that 0.75% of all detected neutrons with incoming energy in the range 200 ± 10 MeV scatter in the upper layer at an angle between 5 and 15 degrees. Note that the overall experimental scattering probability increases monotonically with neutron energy, in contrast to some simulation predictions.

Fig. 12 also includes simulation predictions for neutron scattering angle according to the G4-Physics and MENATE_R models. Data for MENATE_R predictions are split into two plots (the first from 20–80 MeV and the second from 80–200 MeV) for clarity since the predicted scattering probabilities first rise with neutron energy, and then fall at the higher neutron energies, causing overlap for low and high energy data curves. Both models predict a drop in scattering probability for angles near zero degrees for all neutron energies, unlike experimental results that show neutrons above 80 MeV are forward focused.

Fig. 13 shows scattering angle probabilities for a number of neutron energies from 20 to 200 MeV. Plotted data are normalized to the total number of light-producing events of all multiplicities. Note that the MENATE_R model overpredicts probabilities for low neutron energies and underpredicts probabilities for high neutron energies. The energy at which both models are in good agreement with data is around 60 MeV, which is close to the energy at which Kohley et al. conducted their previous test of these same models. Otherwise predictions vary significantly from experiment over the full range of neutron energy for both models.

5. One-neutron scattering signatures and filtering multiple neutron events

A challenge with plastic scintillator arrays has been to filter 2n scattering events from 1n. Two hits in the array can be produced by two separate neutrons, or by a single neutron scattering twice. Tracking of 1n events in plastic scintillator is complicated by the large variety of scattering channels available to neutrons (see Table 1), which include dark-scattering and the creation of additional neutrons and other particles by some of the inelastic channels.

Causal filters can be used to help filter out 1n events based on constraints imposed by energy and momentum conservation on distance and velocity between the first and second hits. Causal filters used by the MoNA group to reduce 1n contributions have typically consisted of gates requiring the distance between hits to be greater than a set minimum, coupled with the requirement that the measured (effective) velocity between hits be above the beam-velocity. Gates using this general approach have been shown to be effective in reducing 1n signals [4–7,10,11]. One drawback to this approach is that it can filter out many 2n events as well. Here we describe two additional filtering approaches that can potentially increase the 2n/1n signal-to-noise factor by allowing more 2n events to survive the causal filter.

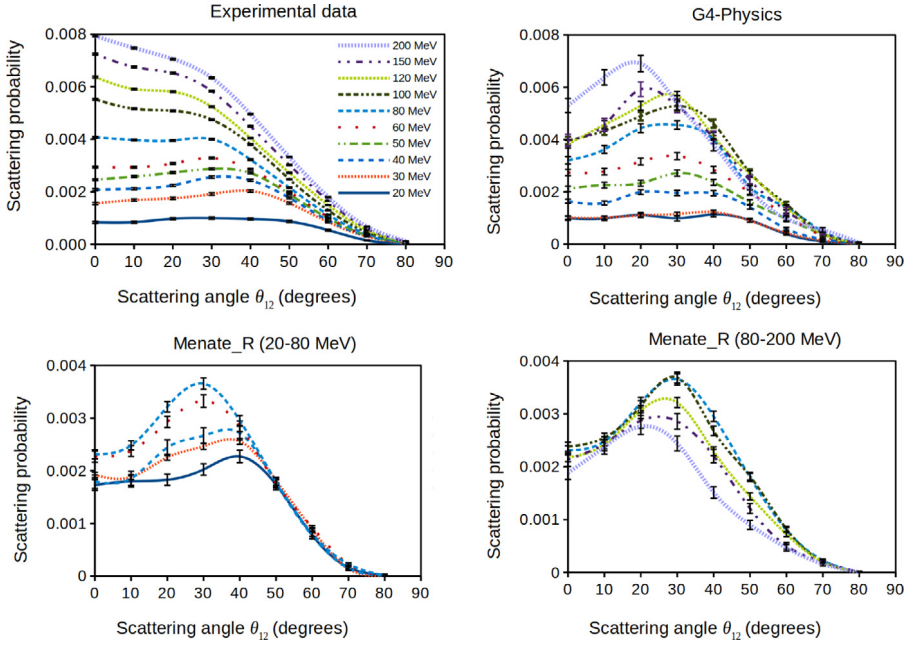

Fig. 12. Neutron scattering probabilities as a function of angle in the upper layer of the array as a function of neutron energy. Shown are experimental results and G4-Physics and MENATE_R model predictions. Plotted on the *y*-axis is the normalized probability relative to the rate for all detected events with multiplicity 1 or greater, and on the *x*-axis is scattering angle, where each data point angle θ corresponds to $\theta \pm 5°$ (horizontal error bars have not been added to this plot for clarity's sake). All error bars are statistical.

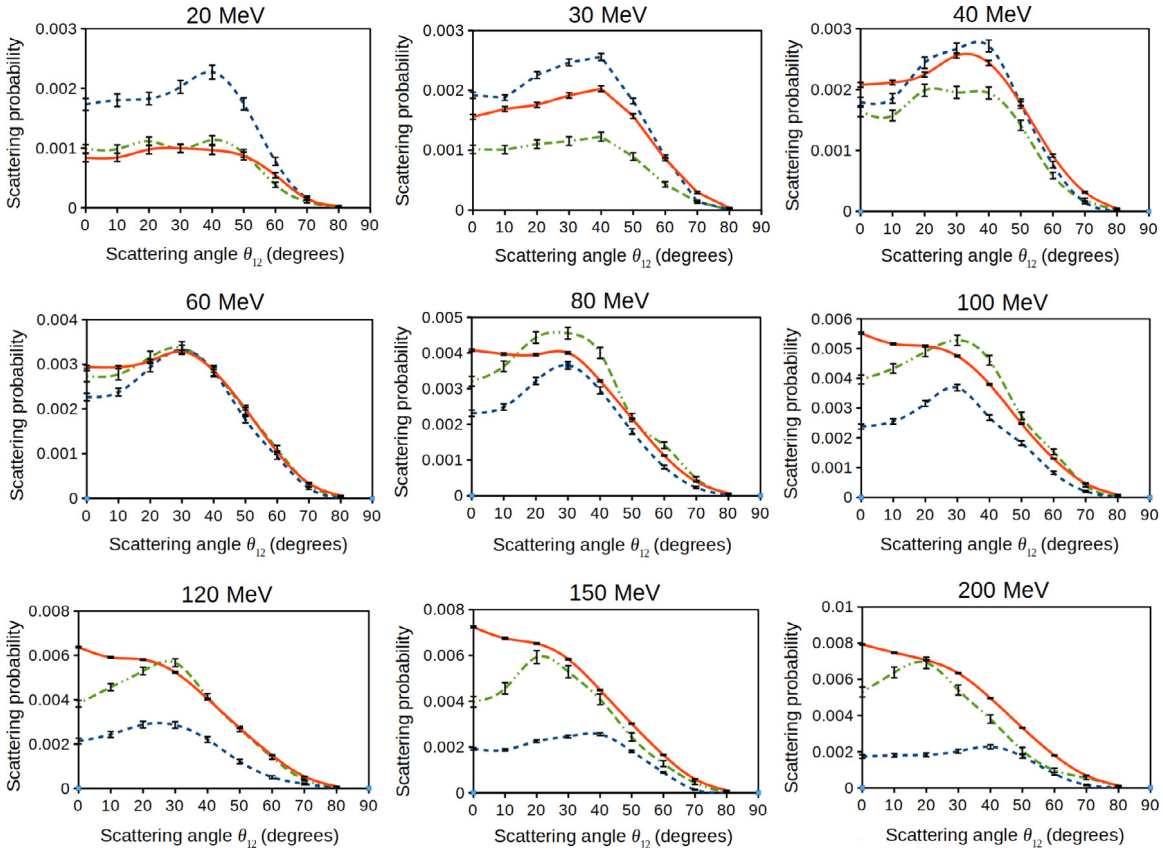

MeV.jpg MeV.jpg

Fig. 13. Neutron scattering probability as a function of scattering angle and neutron energy in the upper layer of the array. Plotted on the *y*-axis is the normalized probability relative to the rate for all detected events with multiplicity 1 or greater (note that upper limit increases with increasing neutron energy), and on the *x*-axis is scattering angle, where each data point angle θ corresponds to $\theta \pm 5°$ (horizontal error bars have not been added to this plot for clarity's sake). Plotted are our experimental observations compared with G4-Physics and MENATE_R model predictions. Solid curves (red) are data, dashed curves (blue) are MENATE_R simulation prediction, and dot-dashed curves (green) are G4-Physics simulation prediction. All error bars are statistical.

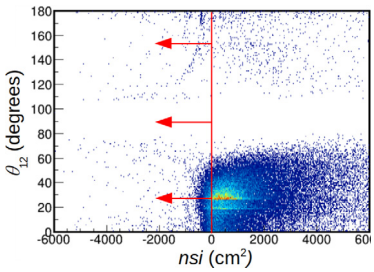

Fig. 14. Plot of neutron scattering angle versus the neutron spacetime interval (*nsi*, defined in Eq. (1)) for 80 MeV incident neutrons. The cluster of 1n scatters is clearly visible the lower portion of the plot. The vertical line and arrows indicate the 2n region allowed by a simple causal filter using neutron beam velocity.

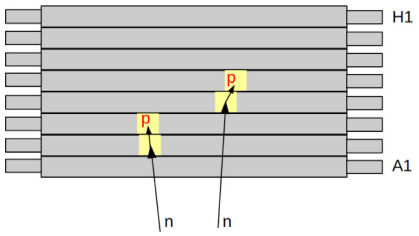

Fig. 15. Schematic of two proton crosstalk events occurring in separate locations in the array, as seen from above.

5.1. Gating with the neutron spacetime interval

The first approach is modeled after the relativistic invariant spacetime interval between two events, $(\Delta s)^2 = (c\Delta t)^2 - r^2$, where Δt is the time between the events, r is the spatial separation between them, and c is the speed of light. Pairs of events with positive spacetime intervals are time-like and can be causally connected by a signal with velocity c or less. Those with negative values are space-like events unable to be causally connected.

We define the neutron spacetime interval *nsi* as

$$nsi = (v_b \Delta t)^2 - r_{12}^2 \quad (1)$$

where v_b is the neutron beam velocity, r_{12} is the pathlength between hits, and Δt is the time between them. In analogy to events connected by the relativistic invariant spacetime interval, pairs of neutron scattering events with positive *nsi* values (time-like) are capable of being causally connected by a single neutron moving at beam velocity or less, whereas those with negative *nsi* values (space-like) are unable to be connected by a single scattered neutron.

Fig. 14 shows a plot of scattering angle θ_{12} versus *nsi* for 80 MeV 1n events. The cluster of 1n scatters is clearly visible the lower portion of the plot. A simple causal filter requiring the measured velocity between hits to be greater than the beam velocity allows only events with negative *nsi* values, shown by the vertical line and arrows in the plot. On the other hand, 2n scatters can in principle populate all areas on this plot, since the two signals they independently produce are not connected by constraints imposed by energy and momentum conservation at the scatter sites, as are those for 1n events.

The manner in which 2n events populate this plot (and the regions outside the left and right boundaries) depends on, among other things, any specific time and/or geometric correlations that exist between the two neutrons, their relative decay energy, and the beam energy. Assuming that 2n events can populate all areas of the plot uniformly, the use of a 2-dimensional veto gate surrounding the 1n cluster should effectively increase the 2n/1n signal-to-noise by a factor of between about 1.6 and 2 compared with the simpler beam velocity causal filter, by allowing 2n events with positive *nsi* to be included. This factor will depend on the size of the 2D gate around the 1n cluster.

5.2. Gating on multiple crosstalk events

A second method to filter 1n events from a multiple-neutron dataset involves making use of crosstalk events, whose relative rate increases with increasing neutron energy (see Fig. 7). Crosstalk events are created when high energy protons produce light in two adjacent detectors. These high energy protons result primarily from charge-exchange scattering of neutrons from H and C nuclei. The outgoing neutron has comparatively low energy compared with the proton, and is nearly incapable of producing another crosstalk event elsewhere in the array. An effective 2n filter could consist of gating on events with two crosstalk events separated by more than a pre-determined distance threshold. Example of such a double crosstalk event is depicted in Fig. 15.

Crosstalk events result from a single neutron scatter, but appear to the DAQ as hit-multiplicity 2. For the 10 cm thick detector bars used in this experiment, crosstalk events make up more than half of all measured hit-multiplicity 2 events for neutrons above 50 MeV, and the crosstalk event rate approaches 1/3 of the hit-multiplicity 1 rate for neutron energies over 150 MeV (see Fig. 7). A gate designed to filter events consisting of two crosstalk scatters at different locations in the array should produce a dataset rich in 2n events. The level of improvement for the 2n/1n signal-to-noise ratio (compared with the simple causal filter described earlier) is difficult to estimate for this filter. It should be significant, given the relative inability of a single neutron to produce two separate crosstalk events. The 2n/1n signal-to-noise should increase with the application of higher light thresholds to the two hits constituting the crosstalk event. Increasing the thresholds also reduces countrate, so a balance between countrate and threshold values could optimize the 2n/1n ratio value with good statistics. Application of this technique should become increasingly effective for higher neutron energies.

An "*or*" combination of the θ_{12} *vs. nsi* filter and the pairs of separated crosstalk events should prove effective in maximizing the 2n/1n signal-to-noise for the analysis of experiments involving multiple-neutron decays.

6. Conclusions

We present results for several single-neutron scattering signatures in BC-408 scintillator for neutrons with energy from 20 to 200 MeV and with well defined trajectory and entry point in the detector array. We compared these results with two Monte Carlo model predictions for neutron interactions with H and C nuclei, the stock G4-Physics package included with GEANT4 [30,31] based on the cascade model for neutron interactions, and MENATE_R [14], a scattering cross section based model used within the GEANT4 framework. Both simulations incorporated the same detector geometry and makeup of the detectors, and the same analysis gates were applied to data and to simulation.

We find agreement between simulation and data to range from good to poor, and highly dependent on neutron energy. First light-producing neutron interactions in the plastic scintillator array are relatively well reproduced by both models over the energy range considered. Note in particular the excellent agreement in reproducing the attenuation depth for the neutron beam first interactions over the entire energy range considered (Fig. 6), and for the relatively good agreement for dark-scattering observations (Fig. 9). While both models over-predict the rate of proton-crosstalk events over the energy range considered, MENATE_R does a better job modeling this observable.

Agreement is poorer for events requiring two or more hits. The lack of agreement for both models in reproducing multiplicity distributions over the energy range considered is shown in Fig. 10. The MENATE_R model does a good job reproducing multiplicity distributions up to multiplicity 4 at energies typical for MoNA experiments at NSCL (40–100 MeV), but much less so above 120 MeV. The G4-Physics model

multiplicity predictions are poor for essentially all energies considered. Both models do a poor job simulating the neutron propagation between hits, as shown in Figs. 11, and 13, pointing to challenges in accurately modeling causal filters applied to 2n datasets, and especially so for higher energies soon to be available at FRIB.

For the scattering results over a broad range of neutron energy reported here, we observe wide variation in the levels of agreement between model predictions and experimental observations. No clear pattern is apparent that might point to specific avenues for simulation improvement. Both models have areas of good agreement and areas of poor agreement compared with experimental observations, and neither shows overall superior performance over the other. Kohley et al. [29] observed that for 55 MeV neutron scattering in BC-408, MENATE_R did a better job at modeling neutron scattering compared with G4-Physics for the observables they considered. They concluded that the large differences between the two model predictions likely arise from the different way in which each treats inelastic neutron scattering from C nuclei.

In order to increase the accuracy of simulation predictions, further experimental efforts are needed to improve available cross section and angular distribution data (on which MENATE_R in particular relies) for 20–200 MeV neutrons scattering inelastically from C nuclei. However the wide variation of agreement over a broad range of neutron energy demonstrated here for both models is not likely to be resolved solely by an improvement in the cross section database. Other improvements to simulation will be important in preparation for future studies at higher neutron energies soon to be available at FRIB.

Comparison with predictions from other neutron transport simulations, such as FLUKA [32,33] and MCNPX [34], both of which are not considered here, would be of great interest since they use different approaches to neutron interaction and propagation in the detector medium. Data presented in this study can be made available upon request for tests of simulation models.

Acknowledgments

The authors would like to thank the physics and engineering staff at LANSCE for the production and maintenance of the pulsed proton beam and the neutron spallation source. We would also like to thank members of the MoNA collaboration for support and helpful conversations. Work presented here is supported by the National Science Foundation (United States of America) grant PHY-1744043, and the Department of Energy (United States of America) National Nuclear Security Administration grant DE-NA0000979 through the Nuclear Science and Security Consortium.

References

[1] T. Baumann, et al., Nucl. Instrum. Methods A 543 (2005) 517.
[2] NeuLAND Technical Design Report, http://www.fair-center.eu/fileadmin/fair/experiments/NUSTAR/Pdf/TDRs/NeuLAND-TDR-Web.pdf.
[3] T. Nakamura, Y. Kondo, Nucl. Instrum. Methods Phys. Res. B 376 (2015) 1.
[4] C.R. Hoffman, et al., Phys. Rev. C 83 (2011) 031303(R).
[5] E. Lunderberg, et al., Phys. Rev. Lett. 108 (2012) 142503.
[6] A. Spyrou, et al., Phys. Rev. Lett. 108 (2012) 102501.
[7] M.D. Jones, et al., Phys. Rev. C 91 (2015) 044312.
[8] <https://frib.msu.edu/>.
[9] M.D. Bird, et al., IEEE Trans. Appl Supercond. 15 (2005) 1252.
[10] J.K. Smith, et al., Nuclear Phys. A 955 (2016) 27.
[11] T. Nakamura, et al., Phys. Rev. Lett. 96 (2006) 252502.
[12] D.A. Kellogg, Phys. Rev. 90 (1953) 224.
[13] A. Del Guerra, Nucl. Instrum. Methods 135 (1976) 337.
[14] B. Roeder, Development and Validation of Neutron Detection Simulations for EURISOL, EURISOL Design Study, Report: [10-25-2008-006-In-beamvalidations.pdf, 31-44] (2008), <http://www.eurisol.org/site02/physics_and_instrumentation/>.
[15] https://www.crystals.saint-gobain.com/sites/imdf.crystals.com/files/documents/bc400-404-408-412-416-data-sheet.pdf.
[16] <https://lansce.lanl.gov/facilities/wnr/index.php>.
[17] <https://lansce.lanl.gov/>.
[18] <https://lansce.lanl.gov/facilities/lujan/index.php>.
[19] R.C. Haight, J. Instrum. 7 (2012) C05002.
[20] Geant4 <http://geant4.web.cern.ch>2011.
[21] http://geant4-userdoc.web.cern.ch/geant4-userdoc/UsersGuides/PhysicsListGuide/BackupVersions/V10.4/html/electromagnetic/Opt3.html.
[22] Japanese Evaluated Nuclear Data Library (JENDL), <http://wwwndc.jaea.go.jp/jendl/jendl.html>.
[23] P. Desesquelles, et al., Nucl. Inst. Meth. A 366 (1991).
[24] P. Rose (Ed.), ENDF/B-VI Summary Document, Report BNL-NCS-17541, National Nuclear Data Center, Brookhaven National Laboratory, 1991.
[25] Evaluated Nuclear Data File (ENDF) <http://www.nndc.bnl.gov/exfor/endf00.jsp>.
[26] Y. Watanabe, et al., Nuclear data evaluations for JENDL high-energy file, in: Proceedings of the International Conference on Nuclear Data for Science and Technology, Vol. 769, AIP Conference Proceedings, 2005, p. 326.
[27] R.A. Cecil, B.D. Anderson, R. Madey, Nucl. Inst. Meth. A 161 (1979) 439.
[28] G.F. Knoll, Radiaton Detection and Measurement, John Wiley & Sons, Inc., 2000.
[29] Z. Kohley, et al., Nucl. Instrum. Methods A 682 (2012) 59.
[30] S. Agostinelli, et al., Nucl. Inst. Meth. A 506 (2003) 250.
[31] J. Allision, et al., IEEE Trans. Nucl. Sci. NS-53 (2006) 270.
[32] G. Battistonie, et al., AIP Conf. Proc. 896 (2007) 31.
[33] FLUKA <http://www.fluka.org>.
[34] MCNPX <http://mcnpx.lanl.gov>.